Materials Horizons

ROYAL SOCIETY OF CHEMISTRY

COMMUNICATION

View Article Online
View Journal

Open Access Article. Published on 08 December 2025. Downloaded on 2/25/2026 3:05:04 AM.
This article is licensed under a Creative Commons Attribution-NonCommercial 3.0 Unported Licence.

Check for updates

Cite this: DOI: 10.1039/d5mh01840d

Received 26th September 2025,
Accepted 5th December 2025

DOI: 10.1039/d5mh01840d

rsc.li/materials-horizons

Synergistic interphase regulation with a KSeCN bifunctional additive for stable and high-performance lithium–sulfur batteries

Junpeng Rao,†[abc] Yuxuan Feng,†[ab] Tong Yu,[a] Ru Xiao,[ab] Yaozu Wang,[ab] Dean Shi,[c] Feng Li *[ab] and Zhenhua Sun *[ab]

Lithium sulfur batteries (LSBs) have good potential for next-generation energy storage. However, the practical applications of LSBs are restricted by the shuttle effect of lithium polysulfides (LiPS) and uncontrollable Li deposition. Here, potassium selenocyanate (KSeCN) is proposed as a bifunctional electrolyte additive that can synergistically regulate both the cathode and anode electrode/electrolyte interfaces due to its optimum orbital energy levels. KSeCN promotes the formation of a hybrid organic–inorganic cathode electrolyte interface (CEI) that inhibits the shuttle effect and boosts the conversion kinetics of LiPS by incorporating conductive Se into the cathode. In addition, KSeCN facilitates an inorganic-rich solid electrolyte interface (SEI), promoting homogeneous Li^+ deposition and suppressing Li dendrite growth. Correspondingly, LSBs with the KSeCN additive achieve a low capacity decay rate of 0.05% per cycle over 1000 cycles with excellent stability, while Li–S pouch cells operate stably for ~140 cycles. Li‖Li symmetric cells exhibit a reduced hysteresis voltage and extended cycling lifetimes exceeding 1000 h. This work demonstrates a promising additive design strategy for high-performance LSBs through interfacial chemistry engineering.

New concepts

This work proposes a bifunctional electrolyte additive, potassium selenocyanate (KSeCN), to synergistically boost the redox kinetics of lithium polysulfides (LiPS) and the cycling stability of the Li anode through interfacial chemical engineering. The electrolyte/electrode interphases are simultaneously regulated due to the optimal molecular orbital energy levels of KSeCN. A Se-induced hybrid organic–inorganic cathode electrolyte interface (CEI) is formed, thereby facilitating the conversion kinetics of LiPS and inhibiting the shuttle effect. Moreover, the presence of KSeCN also promotes the formation of a multicomponent hybrid solid electrolyte interface (SEI) enriched with LiF and Li_3N, which is beneficial for uniform Li^+ deposition, and suppressing the growth of Li dendrites. Consequently, *in situ* EIS investigations along with electrochemical measurements demonstrate the enhanced redox reactions of LiPS and extended operational lifetime in pouch cells. The concept of interfacial engineering through an electrolyte additive offers new insights for the construction of high-performance lithium sulfur batteries.

1. Introduction

The increasing demand for sustainable energy has accelerated the development of advanced lithium-ion batteries. Lithium–sulfur batteries (LSBs) are considered as one of the key candidates for next-generation energy storage devices, having a high theoretical specific capacity (1675 mAh g^{-1}) and energy density (2500 Wh kg^{-1}).[1–4] Furthermore, the natural abundance and environmental friendliness of sulfur further enhance the appeal of LSBs. However, significant challenges impede the commercial viability of LSBs. A primary limitation is the shuttle effect, originating from soluble lithium polysulfides (LiPS), which causes irreversible loss of active materials and consequently limits cycling stability. Simultaneously, the uneven deposition of Li^+ on lithium metal anodes promotes lithium dendrite growth, severely degrading the cycling performance and hindering the practical realization of the potential of LSBs.[5–8]

To solve the above issues, many studies have be done in terms of advanced electrodes, separators and electrolytes.[9–13] Regulating the electrode/electrolyte interphases is a common and effective method to achieve high-performance LSBs among the various strategies for modifying the electrolyte. The interphases, including the cathode electrolyte interphase (CEI) and solid electrolyte interphase (SEI) layers, which form during initial charge–discharge cycling, are critical for LSB operation. Soluble LiPS diffuse into the electrolyte through the CEI layer,

[a] Shenyang National Laboratory for Materials Science, Institute of Metal Research, Chinese Academy of Sciences, Shenyang 110016, China. E-mail: fli@imr.ac.cn, zhsun@imr.ac.cn
[b] School of Materials Science and Engineering, University of Science and Technology of China, Shenyang 110016, China
[c] Ministry of Education Key Laboratory for the Green Preparation and Application of Functional Materials, Hubei Key Laboratory of Polymer Materials, School of Materials Science and Engineering, Hubei University, Wuhan 430062, China
† Co-first authors.

Open Access Article. Published on 08 December 2025. Downloaded on 2/25/2026 3:05:04 AM.
This article is licensed under a Creative Commons Attribution-NonCommercial 3.0 Unported Licence.

leading to the shuttle effect.[14] Moreover, the CEI is also where the deposition of solid-state products (Li_2S_2/Li_2S) occurs, which have a huge impact on the capacity of LSBs.[15–17] Thus, establishing a functional CEI is beneficial for optimizing sulfur cathode performance. An efficient strategy demonstrated the *in situ* construction of a thin and compact CEI through chemical reactions involving LiPS, bis(trifluoromethane)sulfonimide ions and vinylene carbonate. This CEI effectively suppressed LiPS shuttling and maintained high sulfur utilization during cycling.[18,19] On the anode side, the SEI is formed between highly reactive Li metal and the electrolyte, initially preventing further parasitic reactions. However, prolonged cycling promotes inhomogeneity and mechanical fragility within the SEI, leading to the formation of a passivation layer and uneven Li^+ precipitation channels. This not only leads to the continuous consumption of electrolyte, but also worsens the deposition behavior of Li^+, leading to uncontrolled dendrite growth.[20,21] These issues can be solved by increasing the proportion of specific inorganic components in the SEI. A functional-derivative-controlled liquid electrolyte containing 1,1,2,2,3,3-hexafluoropropane-1,3disulfonimide potassium (KHFDF) salt was employed in LSBs. The preferential passivation of the lithium anode by the KHFDF salt yielded a hierarchical SEI structure rich in inorganic components (KF and LiF), which induced dendrite-free lithium deposition.[22] Accordingly, synergistic regulation of the CEI and SEI layers through interfacial engineering presents a viable strategy to simultaneously mitigate polysulfide shuttling and protect the lithium metal anode. Achieving such control is paramount for constructing high-performance LSBs and boosting their commercial applications.

In this work, we proposed potassium selenocyanate (KSeCN) as a bifunctional additive to enhance the performance of LSBs (as shown in Fig. 1). In-depth analysis reveals that KSeCN, with its optimal orbital energy levels, synergistically regulates both the cathode and anode electrode/electrolyte interfaces. At the cathode, KSeCN facilitates the introduction of highly conductive Se into sulfur chains and promotes the formation of an organic–inorganic hybrid CEI layer. This modified CEI significantly boosts the redox reaction kinetics of LiPS and effectively inhibits the shuttle effect. At the anode, KSeCN promotes the generation of a multi-component hybrid SEI layer enriched with inorganic LiF and Li_3N. The inorganic-rich SEI homogenizes Li^+ deposition across the lithium metal surface and mitigates corrosion reactions between the Li anode and electrolyte, thereby suppressing dendrite formation. Consequently, KSeCN-containing cells exhibit an ultralow capacity decay rate of 0.05% per cycle over 1000 cycles at 1C (1C = 1675 mA g^{-1}). Li‖Li symmetrical cells demonstrate stable operation for over 1000 h with a minimal polarization voltage (0.5 mA cm^{-2}, 0.5 mAh cm^{-2}; ∼22 mV). Moreover, KSeCN-enabled Li–S pouch cells achieve extended cycling stability beyond 140 cycles. The good electrochemical results underscore the significant potential of the KSeCN-based additive and interfacial engineering for constructing high-performance LSBs.

2. Results and discussion

Molecular orbital energy levels (highest occupied molecular orbital: HOMO; lowest unoccupied molecular orbital: LUMO) are commonly used to determine the oxidation/reduction ability. The components have the potential to synergistically regulate electrolyte/electrode interfaces if they have orbitals with appropriate energy levels. Accordingly, density functional theory (DFT) calculations of molecular orbitals were performed to elucidate the working mechanism of KSeCN for interphase formation. As shown in Fig. 2a, KSeCN showed the highest HOMO and the lowest

LUMO energy levels among all electrolyte components, indicating its tendency to undergo preferential decomposition at both the cathode and anode.[23,24] Such electronic-structure characteristics suggest that KSeCN, as an additive, can

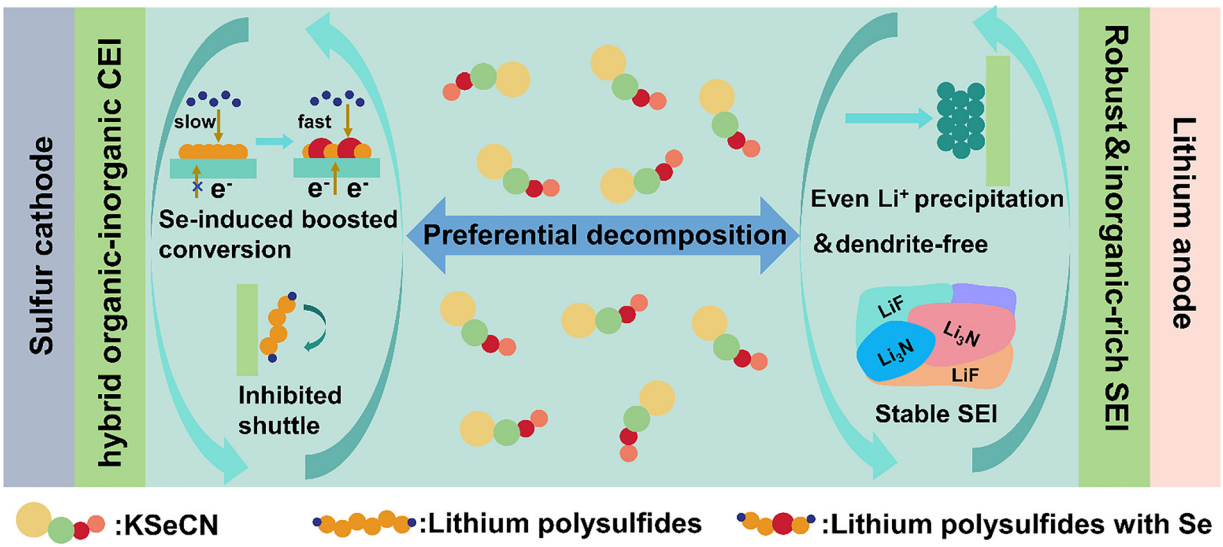

Fig. 1 A schematic diagram of the effect of KSeCN on the electrodes.

Open Access Article. Published on 08 December 2025. Downloaded on 2/25/2026 3:05:04 AM.
This article is licensed under a Creative Commons Attribution-NonCommercial 3.0 Unported Licence.

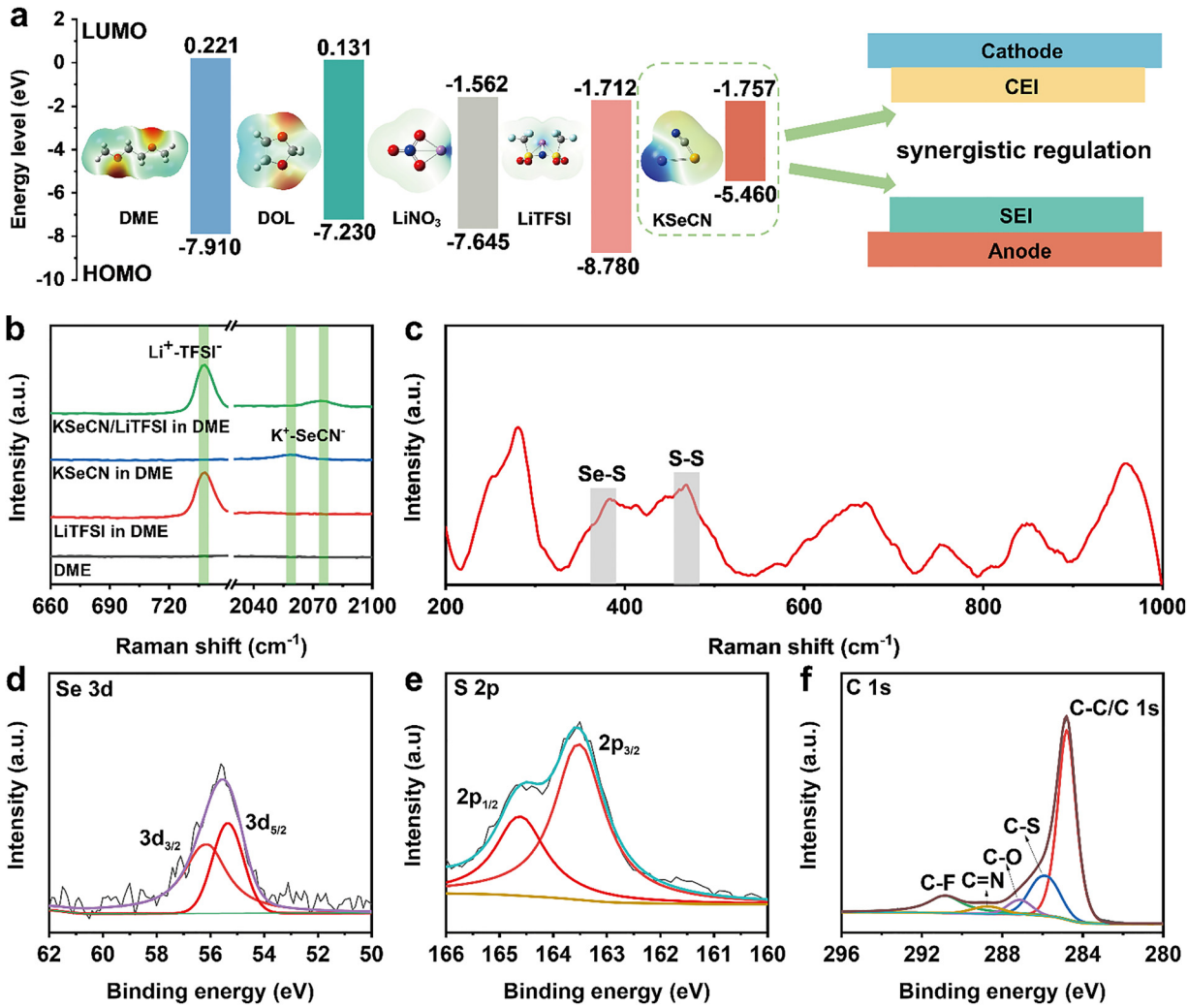

Fig. 2 (a) A comparison of molecular orbital energy levels for all components in the electrolyte. (b) Raman spectra of LiTFSI, KSeCN and LiTFSI with KSeCN in DME. (c) Raman spectra of the cathode from a cycled Li–S cell with KSeCN. (d) Se 3d, (e) S 2p and (f) C 1s XPS results from the cycled cathode with KSeCN.

contribute to the synergistic regulation of the cathode–electrolyte interphase (CEI) and solid–electrolyte interphase (SEI) through the optimized molecular orbital energy levels. To further understand its behavior in solution, the solvation structure of KSeCN in electrolyte was investigated. Raman measurements were performed to probe the coordination environment in various electrolytes. As depicted in Fig. 2b, the Raman spectra show the solvation structures of both the lithium salt and KSeCN in ether-based solvent. The addition of lithium bis(trifluoromethanesulphonyl)imide (LiTFSI) caused a blue shift in the Raman signal corresponding to the Se-CN vibration of KSeCN in 1,2-dimethoxyethane (DME), indicating a reduction in K^+ coordination with $SeCN^-$, resulting in an upshift in the C≡N stretching frequency. This shift suggests that KSeCN is more likely to decompose molecularly.[25] Additionally, ^{7}Li nuclear magnetic resonance (NMR) spectroscopy was employed to examine the solvation of Li^+. As shown in Fig. S1a, the ^{7}Li signal moved downfield in the KSeCN-containing electrolyte, which can be attributed to a deshielding effect. A corresponding decrease in relaxation time was also observed (Fig. S1b), indicating the interactions of Li^+ anions in the KSeCN-modified electrolyte are stronger than in the control one. In addition, *ab initio* molecular dynamics (AIMD) simulations were further conducted to clarify the impact of KSeCN on the solvation structures of Li^+ at a molecular level. As shown in Fig. S2, radial distribution function (RDF) analysis reveals a pronounced peak corresponding to $SeCN^-$ in the inner solvation shell (Fig. S2a). The coordination number (CN) of Li^+ with $SeCN^-$ remained stable within the first solvation shell, confirming the exclusive presence of $SeCN^-$ in this region (Fig. S2b). This solvation structure facilitates the preferential decomposition of anionic $SeCN^-$ during interfacial processes. The spectral results along with theoretical calculations revealed that KSeCN has the potential to synergistically improve the CEI and SEI, thereby boosting the performance of Li–S cells through regulating the electrode/electrolyte interphases.

Furthermore, the chemical bonding environment and components of the CEI layer were investigated to elucidate the influence of KSeCN on the cathode. Fig. 2c shows the Raman spectrum of a cycled cathode from a KSeCN-containing cell.

Open Access Article. Published on 08 December 2025. Downloaded on 2/25/2026 3:05:04 AM.
This article is licensed under a Creative Commons Attribution-NonCommercial 3.0 Unported Licence.

The presence of a Se–S peak (located at 382 cm^{-1}) indicated the involvement of KSeCN in CEI formation and the successful incorporation of Se into the cathode. Time-of-flight secondary ion mass spectrometry (TOF-SIMS) depth profiling (Fig. S3) further confirms the incorporation of Se into the cathode surface layer. Strong Se^{2-} signals remained in the KSeCN-containing cell, while only background levels are detected in the KSeCN-free cell. Elemental distribution analysis of the cycled cathodes further confirmed the uniform dispersion of Se (Fig. S4). Given that selenium exhibits higher electrical conductivity than sulfur, the introduction of Se is beneficial for enhancing the reaction kinetics of polysulfides, leading to improved battery performance.[26] The CEI layer was further examined *via* X-ray photoelectron spectroscopy (XPS). The XPS results (Fig. S5) also verified the presence of Se. Fig. 2d and e displays the deconvoluted Se 3d and S 2p spectra of the cycled cathode. The peaks at 56.1 eV and 55.3 eV in Fig. 2d are assigned to Se–S bonds, while those peaks at 164.5 eV and 163.3 eV in Fig. 2e correspond to S–S/S–Se bonds, consistent with the Raman findings.[27] Moreover, the appearance of new peaks in the S 2s XPS results (Fig. S6) also indicated the participation of Se in sulfur evolution. Notably, in addition to the characteristic C–C peak (284.8 eV) in the C 1s spectrum (Fig. 2f and Fig. S7), several other peaks associated with carbon-containing bonds were observed, indicating the formation of an organic–inorganic hybrid CEI layer. TEM combined with EDS mapping (Fig. S8) visually demonstrates a uniform CEI layer on cycled S/C particles, with Se homogeneously distributed alongside C and S, confirming the integration of Se into the CEI. Since polysulfide diffusion initiates at the electrode/electrolyte interface, such a functional organic–inorganic hybrid CEI is expected to effectively suppress the shuttle effect of LiPS.

The conversion kinetics of polysulfides were subsequently studied to elucidate the positive effect of the KSeCN additive on the performance of Li–S cells. First, the ionic conductivity of electrolytes was investigated using stainless-steel symmetrical cells. As shown in Fig. 3a, the electrolyte containing KSeCN

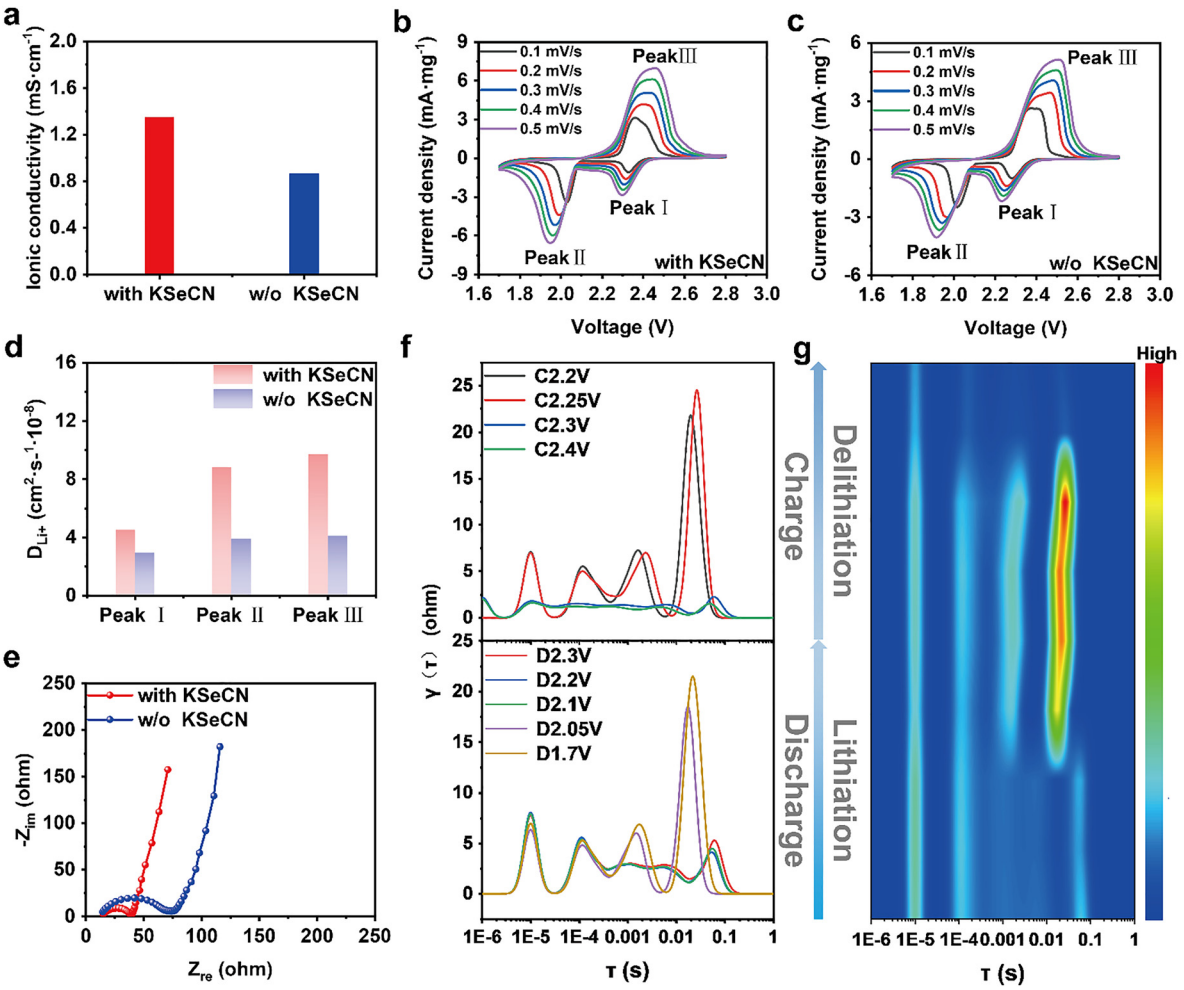

Fig. 3 (a) Ionic conductivities of electrolytes with and without KSeCN. (b) CV curves of Li–S cells with KSeCN at different scan rates. (c) CV curves of Li–S cells without KSeCN at different scan rates. (d) The fitted Li^+ diffusion coefficients from CV curves. (e) The EIS results of Li–S cells with and without KSeCN at the open circuit voltage. (f) DRT data calculated from EIS measurements of cells with KSeCN at different voltages. (g) The corresponding contour plot from DRT analysis of cells with KSeCN.

Open Access Article. Published on 08 December 2025. Downloaded on 2/25/2026 3:05:04 AM.
This article is licensed under a Creative Commons Attribution-NonCommercial 3.0 Unported Licence.

displayed higher ionic conductivity (1.35 mS cm^{-1}) compared with the control electrolyte (0.83 mS cm^{-1}), which indicated the improved migration of Li^+. To further investigate the conversion kinetics and Li^+ transport, variable-speed cyclic voltammetry (CV) was carried out with a scan rate range of 0.1–0.5 mV s^{-1}. Three distinct redox peaks are observed, attributed to different reaction stages in the Li–S system. The two cathodic peaks, designated as Peak I and Peak II, are associated with the reduction processes of S_8 to soluble Li_2S_n (n = 8, 6, or 4) and subsequent conversion to Li_2S_2/Li_2S, respectively. The anodic peak, Peak III, corresponds to the oxidation of Li_2S back to S_8.[28,29] Upon increasing the scan rate, all peak currents were raised and the polarization became more pronounced, consistent with fundamental electrochemical principles. Notably, the cells with KSeCN showed higher peak currents and reduced voltage polarization, suggesting that it facilitated the conversion of lithium polysulfides and enhanced the reaction kinetics. The lithium-ion diffusion coefficient (D_{Li+}) values were derived from the CV data based on the linear relationship between the peak current (I_p) and the square root of the scan rate ($v^{0.5}$), in accordance with the following Randles–Sevcik equation:

$$I_p = 2.69 \times 10^5 n^{1.5} A D_{Li}^{0.5} v^{0.5} C_{Li}$$

where n is the number of transferred electrons, A is the electrode area, and C_{Li} is the concentration of Li^+.[30,31] As shown in Fig. 3d and Fig. S9, D_{Li+} values for Peaks I, II and III in cells with KSeCN were calculated to be 4.51×10^{-8}, 8.18×10^{-8}, and 9.72×10^{-8} cm^2 s^{-1}, respectively, which are significantly higher than those of control cells (2.93×10^{-8}, 3.91×10^{-8} and 4.10×10^{-8} cm^2 s^{-1}). These results confirm that the incorporation of KSeCN facilitates faster and more-efficient Li^+ diffusion during charge/discharge processes, thereby corroborating its beneficial role in improving the LiPS conversion kinetics.

To better understand the redox conversion kinetics of polysulfides during cycling, galvanostatic intermittent titration technique (GITT) measurements were performed at 0.2C to access the internal resistance associated with Li_2S nucleation and activation. As revealed in Fig. S10, the cells containing KSeCN exhibited smaller voltage hysteresis during Li_2S nucleation and activation, indicating reduced polarization and improved polysulfide kinetics. This enhancement is attributed to the incorporation of highly conductive Se and the formation of a robust CEI resulting from the decomposition of KSeCN. *In situ* XRD measurements were then conducted to directly monitor the phase evolution of sulfur during cycling. As shown in Fig. S11, crystalline α-S_8 (~23°) was detected in both cells and disappeared when ~20% depth of discharge (DOD) was achieved, corresponding to conversion from S_8 to LiPS. A peak appearing at ~27° between 40% DOD and 60% DOD is associated with crystalline cubic Li_2S. The cells with KSeCN exhibited a broader Li_2S peak width than the cells without KSeCN, indicating significantly promoted Li_2S nucleation kinetics. The nucleation behavior of Li_2S was further investigated to evaluate its deposition kinetics. As shown in Fig. S12a and S12b, a higher current response was observed in cells with KSeCN, suggesting improved conversion efficiency from soluble LiPS to solid Li_2S. In addition, the current–time curve was derived from the nucleation curve, as presented in Fig. S12e. The nucleation and growth processes of Li_2S in KSeCN-containing cells closely follow the three-dimensional progressive (3DP) model, indicating a higher deposition capacity and delayed passivation layer formation. Scanning electron microscope (SEM) images (Fig. S12c and S12d) showing the Li_2S growth morphology further confirmed the 3D pattern of nucleated Li_2S, which is expected to improve sulfur utilization and enhance the overall electrochemical performance.[32]

Fig. 3e shows the electrochemical impedance spectroscopy (EIS) results from cells obtained at the open circuit voltage (OCV). The overall impedance of a cell with KSeCN was lower than that of a cell without the additive, indicating accelerated reaction kinetics. Furthermore, *in situ* EIS measurements were also carried out during the first charge/discharge cycle to monitor the evolution of the electrode kinetics. The EIS data was further analyzed using the distribution of relaxation time (DRT) method to quantify the time constants and correlate them with specific electrochemical processes. During cycling, four distinct peaks were identified in the DRT curves (Fig. 3f): D1 (10^{-5} to 10^{-4}), D2 (10^{-4} to 10^{-3}), D3 (10^{-3} to 10^{-2}), and D4 (10^{-2} to 1). The D1 peak is related to sulfide grain boundary resistance, which reflects contact resistance at the collector/electrode interfaces and between electrode particles. The D2 and D3 peaks correspond to ion transport across the anode and cathode interfaces, respectively. The D4 peak, which has the largest time constant (a frequency below 0.1 Hz), is related to solid-state diffusion and charge transfer at the sulfur cathode. In the cells with KSeCN, all DRT peak intensities remained relatively low during cycling. The D4 peak intensity increased between 2.1 V and 2.05 V during discharge, which can be attributed to the nucleation of insulating Li_2S, reducing charge transfer.[33–35] In contrast, during charging, the D4 peak intensity gradually decreased, especially above 2.25 V, corresponding to the oxidation of Li_2S to LiPS and finally to S_8, which is beneficial for charge transfer (Fig. 3g). By comparison, the cells without KSeCN exhibited significantly higher DRT intensities throughout cycling, with pronounced increases in the D3 and D4 peaks (Fig. S13). These results further demonstrate the beneficial role of KSeCN in interfacial modification: the introduced conductive Se and the formation of a high-quality organic–inorganic hybrid CEI layer boosted the redox reaction kinetics of polysulfides.

Due to the preferential characteristics of KSeCN for decomposition on the electrode surface, which is likely to alter the chemical composition of the interface layers, the influence of KSeCN on Li^+ plating/stripping behavior was further investigated using electrochemical and interfacial analytical methods. Li‖Li symmetric cells were first assembled to evaluate the cycling performance. As shown in Fig. 4a and b, the cell without KSeCN showed intense voltage fluctuations and high overpotentials, especially after cycling for ~200 h. These phenomena can be attributed to the fracturing of the unstable SEI, which exposed the Li anode to electrolyte, ultimately resulting in the

Open Access Article. Published on 08 December 2025. Downloaded on 2/25/2026 3:05:04 AM.
This article is licensed under a Creative Commons Attribution-NonCommercial 3.0 Unported Licence.

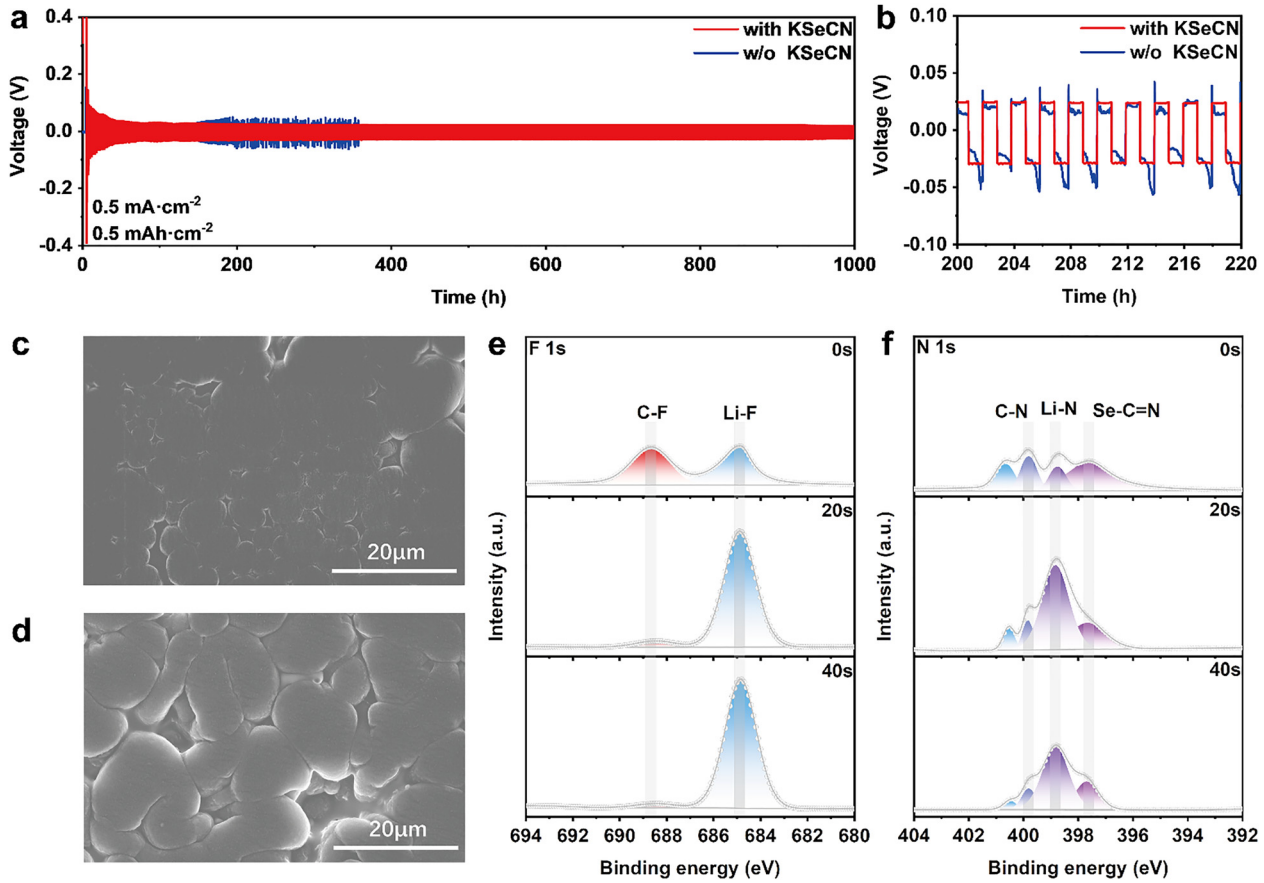

Fig. 4 (a) Galvanostatic curves of Li–Li cells with and without KSeCN. (b) A localized magnified image of overpotential. SEM images of cycled Li metal in Li–Li cells (c) with and (d) without KSeCN. (e) F 1s spectra of the cycled Li anode surface at different depths in KSeCN-containing cells. (f) N 1s spectra of the cycled Li anode surface at different depths in KSeCN-containing cells.

uncontrolled growth of lithium dendrites. In contrast, cells containing KSeCN maintained a low hysteresis voltage of only 22 mV and remained stable for over 1000 h. The improved performance is primarily owing to the formation of a robust SEI, which promotes homogeneous Li^+ plating/stripping and reduces hysteresis polarization. To further investigate the Li^+ deposition behavior, the morphologies of cycled Li anodes were further examined using SEM. As shown in Fig. 4c, the surface of Li metal in the cell with KSeCN remained uniform and compact. In addition, no lithium dendrites were observed, which suggested uniform Li^+ deposition. On the other hand, the lithium surface in the KSeCN-free cell (Fig. 4d) exhibited numerous cracks and considerable roughness, indicating uneven Li^+ precipitation.

To elucidate the origin of the improved Li^+ deposition behavior in cells with KSeCN, the chemical composition of the SEI on the lithium metal surface was analyzed *via* XPS. Fig. S14 shows the atomic profiles in SEI layers with and without KSeCN. The proportions of F and N atoms were rather higher in the presence of KSeCN, indicating the formation of an inorganic-rich SEI layer in KSeCN-containing cells. This type of SEI is beneficial for Li^+ deposition owing to its high ionic conductivity. To identify the specific chemical species, the F 1s and N 1s spectra were further deconvoluted. In the F 1s spectrum (Fig. 4e), two distinct peaks were observed at 684.8 eV and 688.7 eV, corresponding to LiF and C–F, respectively.[36] LiF primarily originated from the decomposition of LiTFSI, and the content increased with sputtering time. Moreover, the LiF content was considerably higher in cells with KSeCN than in the control cells (Fig. S15). After 40 s of XPS depth profiling, the LiF content in the cell with KSeCN increased to 2.1 times the initial surface value, compared to 1.7 times in the KSeCN-free cell, confirming the formation of a more inorganic-rich SEI in the former case. LiF has high interfacial energy, high ionic conductivity and is a good electrical insulator, all of which facilitate Li^+ plating/stripping and suppress lithium dendrite growth. In addition, as shown in Fig. 4f, the N 1s spectrum revealed the presence of various nitrogen-containing species, including Li_3N (398.8 eV), which is formed through a decomposition reaction between KSeCN and Li salts (like $LiNO_3$).[25,37] The XPS results collectively indicate that the incorporation of KSeCN promotes the formation of an inorganic-rich SEI layer on the lithium metal surface, which homogenized Li^+ deposition and inhibited dendrite growth.

Owing to the cooperative effect of KSeCN on the stabilization of both the SEI and CEI layers, Li-S cells incorporating KSeCN as an additive exhibit significantly enhanced electrochemical performance. As illustrated in Fig. 5a, the cycling performance

Open Access Article. Published on 08 December 2025. Downloaded on 2/25/2026 3:05:04 AM.
This article is licensed under a Creative Commons Attribution-NonCommercial 3.0 Unported Licence.

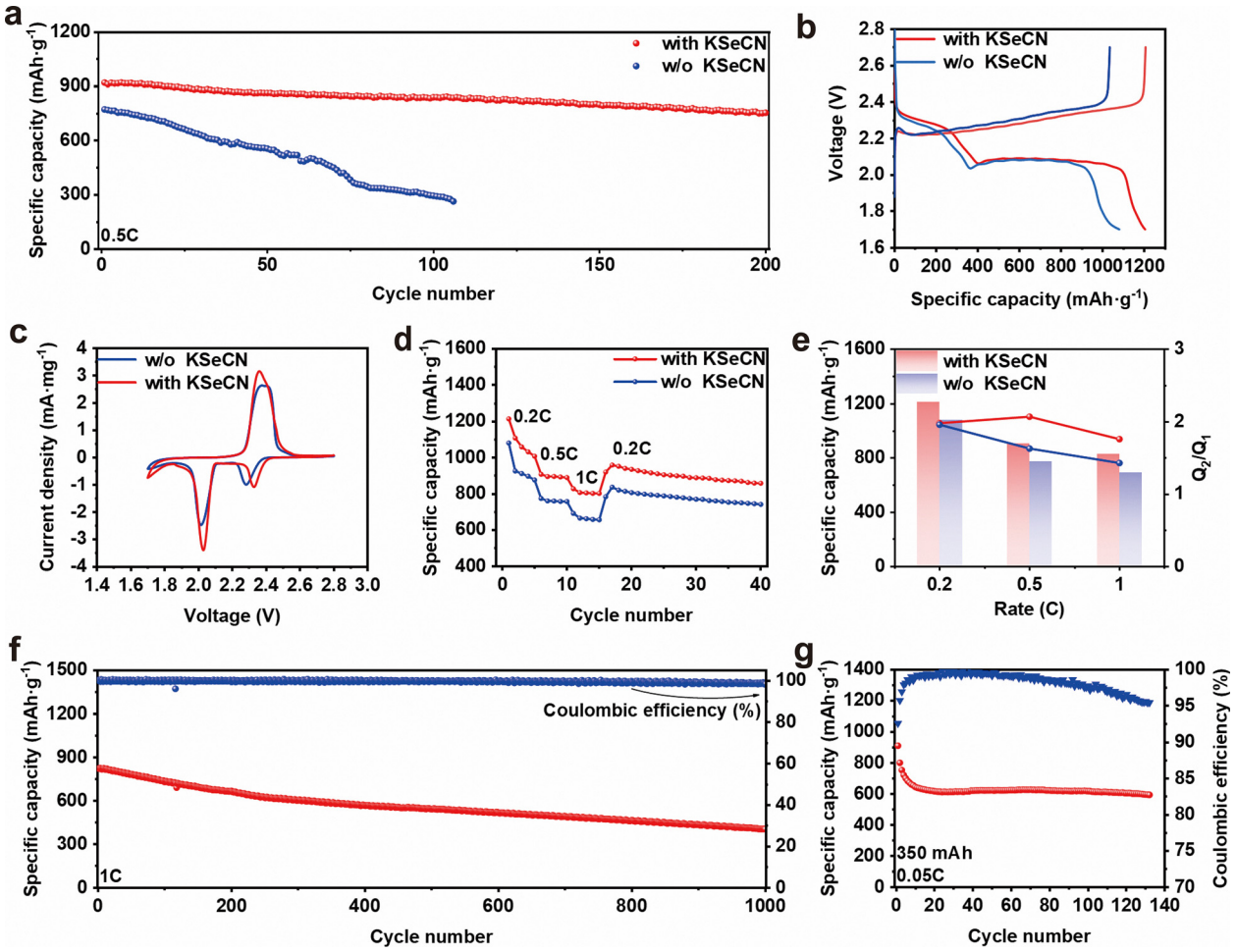

Fig. 5 (a) The long-term cycling performance of Li–S cells with and without KSeCN at 0.5C. (b) The charge–discharge curves of Li-S cells with and without KSeCN at 0.2C. (c) The CV curves of cells with and without KSeCN at 0.1 mV s^{-1}. (d) The rate performance of Li–S cells with and without KSeCN. (e) A comparison of specific capacity at different current densities. (f) The cycling performance of a cell with KSeCN at 1C. (g) The cycling performance of Li–S pouch cell with KSeCN.

was evaluated at 0.5C. The cell with KSeCN maintained a high reversible capacity retention of 82.6% after 200 cycles, which means the effective suppression of the polysulfide shuttle effect due to the formation of an organic–inorganic hybrid CEI layer. The corresponding charge–discharge profiles in Fig. 5b further revealed the reduced polarization voltage in the KSeCN-containing cells, indicating improved LiPS conversion kinetics. Fig. 5c depicts the CV curves of cells with different electrolytes, scanned at 0.1 mV s^{-1}. The redox peaks of the KSeCN-containing cell showed higher current responses compared with those without KSeCN. Furthermore, the reduction peaks are positively shifted, indicating reduced polarization and enhanced redox kinetics in cells with the KSeCN additive. The rate capability was further investigated at various current densities from 0.2C to 1C (Fig. 5d). The KSeCN-containing cell delivered superior rate capacities of 1213.6, 907.2 and 827.7 mAh g^{-1} at 0.2C, 0.5C and 1C, respectively, outperforming the control cell, which exhibited capacities of 1080.2, 773.8, 691.5 mAh g^{-1}. These results underscore the accelerated polysulfide conversion kinetics. The charge–discharge curves in Fig. S16 also exhibited longer capacity platforms (denoted as Q1 for $S_8 \rightarrow Li_2S_n$ and Q2 for $Li_2S_n \rightarrow Li_2S_2/Li_2S$) along with lower polarization voltages.[38,39] In addition, KSeCN-containing cells exhibit higher Q2/Q1 ratios (Fig. 5e), which are associated with improved reaction kinetics and higher sulfur utilization. EIS analysis was performed after cycling to elucidate the reaction kinetics. The Nyquist plots in Fig. S17 showed two depressed semicircles in the high- and medium-frequency regions accompanied by a sloping line in the lower-frequency region, which can be fitted to give the bulk resistance (R_b), surface resistance (R_s), and charge-transfer resistance (R_{ct}), respectively.[40,41] The reduced R_{ct} values of KSeCN-containing cells prove the enhanced reaction kinetics of LiPS. In addition, the lower R_s value suggests less accumulation of irreversible dead sulfur, thereby improving sulfur utilization.[42]

To further explore the cycling advantages of KSeCN-containing cells, Fig. 5f depicts the long-term cycling performance of the KSeCN-containing cell at 1C. The cell exhibited an initial capacity of 823.3 mAh g^{-1} and retained 404.7 mAh g^{-1} after 1000 cycles, corresponding to a low decay rate of 0.05%

Open Access Article. Published on 08 December 2025. Downloaded on 2/25/2026 3:05:04 AM.
This article is licensed under a Creative Commons Attribution-NonCommercial 3.0 Unported Licence.

per cycle and an average Coulombic efficiency of approximately 99%. The excellent long-term cycling performance indicates that the polysulfide shuttle effect is effectively suppressed *via* the formation of a stable organic–inorganic hybrid CEI layer. Fig. S18 further presents the cycling performance at high sulfur loading of 5.8 mg cm^{-2}. The KSeCN-containing cell retained a capacity of 533.1 mAh g^{-1} after 90 cycles. Additionally, pouch cells were evaluated to assess the practical applicability. As shown in Fig. 5g, a pouch cell with a total sulfur loading of 208 mg maintained 65.4% of its initial capacity after 140 cycles, demonstrating the potential of KSeCN for practical applications. The comparison of KSeCN with other Se-based additives shown in Table S1 also illustrated the obtained improvements in both the cathodic redox kinetics and anodic cycling stability.

The fundamental findings in this work provide new insights into design strategies for functional electrolyte additives for use in LSBs. The regulation of SEI and CEI layers through an interfacial engineering method involving the preferential decomposition of KSeCN synergistically improved both the cathodic and anodic cycling performance, which is significant for the practical application of LSBs.

3. Conclusions

In summary, this study demonstrates the potential of interfacial engineering for constructing high-performance LSBs through the use of KSeCN as an electrolyte additive. The synergistic preferential decomposition of KSeCN on both electrodes simultaneously regulates the CEI and SEI layers. On the cathode side, highly conductive Se is incorporated, forming an organic–inorganic hybrid CEI that enhances the kinetics of LiPS conversion and suppresses the shuttle effect. On the anode side, the formation of an inorganic-rich SEI optimizes the Li^+ deposition behavior, leading to more uniform lithium plating and inhibited dendrite growth. Consequently, the KSeCN-modified electrolyte exhibits good electrochemical performance for extending the cycling life and stability of LSBs. This work underscores the critical role of KSeCN for enhancing interfacial chemistry and boosting battery performance, offering new insights into additive design for the practical commercial application of LSBs.

Author contributions

Junpeng Rao: writing – review & editing, writing – original draft, validation, methodology, investigation, conceptualization. Yuxuan Feng: writing – review & editing, validation, methodology, investigation, conceptualization. Tong Yu: writing – review & editing, methodology, formal analysis. Ru Xiao: writing – review & editing, methodology, investigation. Yaozu Wang: writing – review & editing, methodology, investigation. Dean Shi: writing – review & editing, supervision, project administration, conceptualization. Feng Li: writing – review & editing, supervision, project administration, funding acquisition, conceptualization. Zhenhua Sun: writing – review & editing, supervision, project administration, funding acquisition, conceptualization.

Conflicts of interest

The authors declare no conflicts of interest.

Data availability

The data supporting this article have been included within the manuscript and supplementary information (SI). The supplementary information contains detailed experimental procedures, additional electrochemical performance as well as analyses of supplementary XPS, TOF-SIMS and *in situ* XRD measurements, along with SEM and TEM images. See DOI: https://doi.org/10.1039/d5mh01840d.

Acknowledgements

The authors acknowledge financial support from the National Key Research and Development Program of China (No. 2024YFE0209500), National Natural Science Foundation of China (No. 22379151, 52020105010), and the Liaoning Province Applied Basic Research Program (2025JH2/101330136).

References

1 S. Chu, Y. Cui and N. Liu, *Nat. Mater.*, 2017, **16**, 16.
2 A. Manthiram, Y. Fu, S.-H. Chung, C. Zu and Y.-S. Su, *Chem. Rev.*, 2014, **114**, 11751.
3 P. G. Bruce, S. A. Freunberger, L. J. Hardwick and J. M. Tarascon, *Nat. Mater.*, 2012, **11**, 19.
4 X.-Y. Li, M. Zhao, Y.-W. Song, C.-X. Bi, Z. Li, Z.-X. Chen, X.-Q. Zhang, B.-Q. Li and J.-Q. Huang, *Chem. Soc. Rev.*, 2025, **54**, 4822.
5 Z. Liang, J. Shen, X. Xu, F. Li, J. Liu, B. Yuan, Y. Yu and M. Zhu, *Adv. Mater.*, 2022, **34**, 2200102.
6 K. Liu, Z. Wang, L. Shi, S. Jungsuttiwong and S. Yuan, *J. Energy Chem.*, 2021, **59**, 320.
7 C. Zhang, R. Du, J. J. Biendicho, M. Yi, K. Xiao, D. Yang, T. Zhang, X. Wang, J. Arbiol, J. Llorca, Y. Zhou, J. R. Morante and A. Cabot, *Adv. Energy Mater.*, 2021, **11**, 2100432.
8 V. K. Tomer, O. A. T. Dias, A. M. Gouda, R. Malik and M. Sain, *Mater. Horiz.*, 2024, **11**, 3090.
9 Z. Li, J. Wang, H. Yuan, Y. Yu and Y. Tan, *Adv. Funct. Mater.*, 2024, **34**, 2405890.
10 L. Zhou, D. L. Danilov, R.-A. Eichel and P. H. L. Notten, *Adv. Energy Mater.*, 2021, **11**, 2001304.
11 Y. T. Liu, Y. Elias, J. S. Meng, D. Aurbach, R. Q. Zou, D. G. Xia and Q. Q. Pang, *Joule*, 2021, **5**, 2323.
12 C. Sun, Y. Liu, J. Sheng, Q. Huang, W. Lv, G. Zhou and H.-M. Cheng, *Mater. Horiz.*, 2020, **7**, 2487.
13 L. Ren, P. Zou, L. Wang, Y. Jing and H. L. Xin, *Energy Mater. Devices*, 2024, **2**, 9370049.
14 X. Xing, Y. J. Li, X. F. Wang, V. Petrova, H. D. Liu and P. Liu, *Energy Storage Mater.*, 2019, **21**, 474.

Open Access Article. Published on 08 December 2025. Downloaded on 2/25/2026 3:05:04 AM.
This article is licensed under a Creative Commons Attribution-NonCommercial 3.0 Unported Licence.

15 Y. Y. Dong, M. Q. Wu, D. Cai, P. Ying, H. T. Ning, M. L. Shu, S. Yang, X. M. Zhou, H. G. Nie, D. Chen, R. Q. Lian and Z. Yang, *Energy Storage Mater.*, 2025, **74**, 103937.
16 Z. Shadike, S. Tan, Q.-C. Wang, R. Lin, E. Hu, D. Qu and X.-Q. Yang, *Mater. Horiz.*, 2021, **8**, 471.
17 X. Zhang, X. Zhang, X. Wang, G. Cui, H. Pan and W. Sun, *Energy Environ. Sci.*, 2025, **18**, 3553.
18 C.-D. Qiu, Y. Hu, K. Cao, X. Wu, B.-H. Huang, J. Liu, Y.-X. Wang, L. Luo, D. Gu, X. Ai, Y. Cao, S. Chen and F.-S. Ke, *Adv. Energy Mater.*, 2023, **13**, 2300229.
19 Y. Chen, Y. Huang, Q. Xu, L. Yang, N. Jiang and S. Yin, *Mater. Horiz.*, 2024, **11**, 6443.
20 H. Zhang, Z. Zeng, F. Ma, Q. Wu, X. Wang, S. Cheng and J. Xie, *Angew. Chem., Int. Ed.*, 2023, **62**, e202300771.
21 Y. X. Yao, X. Chen, C. Yan, X. Q. Zhang, W. L. Cai, J. Q. Huang and Q. Zhang, *Angew. Chem., Int. Ed.*, 2021, **60**, 4090.
22 Y. Jiao, S. Wang, Y. Ma, M. Zhou, L. Zhang, H. Zhang, T. Lei, Y. Di, C. Yan, W. Chen, D. Chen, J. Huang, Y. Hu and Y. Yan, *Adv. Energy Mater.*, 2023, **13**, 2301233.
23 X. Lv, Z. Qian, X. Zhang, X. Zhang, H. Zheng, M. Liu, Y. Liu and J. Lu, *Angew. Chem., Int. Ed.*, 2024, **63**, e202405880.
24 R. Meng, X. He, S. J. H. Ong, C. Cui, S. Song, P. Paoprasert, Q. Pang, Z. J. Xu and X. Liang, *Angew. Chem., Int. Ed.*, 2023, **62**, e202309046.
25 J. Jung, H. Chu, I. Kim, D. H. Lee, G. Doo, H. Kwon, W. Jo, S. Kim, H. Cho and H.-T. Kim, *Adv. Sci.*, 2023, **10**, 2301006.
26 A. Abouimrane, D. Dambournet, K. W. Chapman, P. J. Chupas, W. Weng and K. Amine, *J. Am. Chem. Soc.*, 2012, **134**, 4505.
27 F. F. Liu, L. F. Wang, Z. W. Zhang, P. C. Shi, Y. Z. Feng, Y. Yao, S. F. Ye, H. Y. Wang, X. J. Wu and Y. Yu, *Adv. Funct. Mater.*, 2020, **30**, 2001607.
28 N. N. Wang, X. Zhang, Z. Y. Ju, X. W. Yu, Y. X. Wang, Y. Du, Z. C. Bai, S. X. Dou and G. H. Yu, *Nat. Commun.*, 2021, **12**, 4519.
29 T. P. Zhang, F. Y. Hu, W. L. Shao, S. Y. Liu, H. Peng, Z. H. Song, C. Song, N. Li and X. G. Jian, *ACS Nano*, 2021, **15**, 15027.
30 Y. S. Zhou, Z. Y. Wei, W. W. Lei, J. You, T. Q. Liang, Q. C. Zhang and D. A. Shi, *ACS Appl. Energy Mater.*, 2022, **5**, 7432.
31 H. Yuan, J. Zheng, G. Lu, L. Zhang, T. Yan, J. Luo, Y. Wang, Y. Liu, T. Guo, Z. Wang, J. Nai and X. Tao, *Adv. Mater.*, 2024, **36**, 2400639.
32 J. Rao, T. Yu, Y. Zhou, R. Xiao, Y. Wang, Z. Qu, D. Shi, Z. Sun and F. Li, *Chem. Eng. J.*, 2024, **498**, 155807.
33 Q. Liang, S. Wang, X. Lu, X. Jia, J. Yang, F. Liang, Q. Xie, C. Yang, J. Qian, H. Song and R. Chen, *ACS Nano*, 2024, **18**, 2395.
34 R. Soni, J. B. Robinson, P. R. Shearing, D. J. L. Brett, A. J. E. Rettie and T. S. Miller, *Energy Storage Mater.*, 2022, **51**, 97.
35 Y. Lu, C.-Z. Zhao, J.-Q. Huang and Q. Zhang, *Joule*, 2022, **6**, 1172.
36 Z. Yu, P. E. Rudnicki, Z. Zhang, Z. Huang, H. Celik, S. T. Oyakhire, Y. Chen, X. Kong, S. C. Kim, X. Xiao, H. Wang, Y. Zheng, G. A. Kamat, M. S. Kim, S. F. Bent, J. Qin, Y. Cui and Z. Bao, *Nat. Energy*, 2022, **7**, 94.
37 S. Wang, B. Lu, D. Cheng, Z. Wu, S. Feng, M. Zhang, W. Li, Q. Miao, M. Patel, J. Feng, E. Hopkins, J. Zhou, S. Parab, B. Bhamwala, B. Liaw, Y. S. Meng and P. Liu, *J. Am. Chem. Soc.*, 2023, **145**, 9624.
38 C. Qi, M. Cai, Z. Li, J. Jin, B. V. R. Chowdari, C. Chen and Z. Wen, *Chem. Eng. J.*, 2020, **399**, 125674.
39 H. Al Salem, G. Babu, C. V. Rao and L. M. R. Arava, *J. Am. Chem. Soc.*, 2015, **137**, 11542.
40 X. Lv, Q. Yang, X. Zhang, J. Song, W. Guo and Q. Wang, *Angew. Chem., Int. Ed.*, 2022, **61**, e202213160.
41 J.-Y. Wei, X.-Q. Zhang, L.-P. Hou, P. Shi, B.-Q. Li, Y. Xiao, C. Yan, H. Yuan and J.-Q. Huang, *Adv. Mater.*, 2020, **32**, 2003012.
42 L. Zhao, F. Qiu, X. Deng, Y. Huang, Y. Li, C. Zhao, W. Ren, C. Zou, X. Li, M. Wang and Y. Lin, *ACS Appl. Energy Mater.*, 2022, **5**, 7617.